[18] High-Content Kinetic Calcium Imaging in Drug-Sensitive and Drug-Resistant Human Breast Cancer Cells

By MARIA A. DEBERNARDI and GARY BROOKER

Department of Biology, Integrated Imaging Center
Johns Hopkins University, Montgomery
County Campus, Rockville, Maryland

Abstract

Intracellular calcium $(Ca^{2+})_i$ is involved in the regulation of a variety of biological functions in cancer cells, including growth inhibition, tumor invasiveness, and drug resistance. To gain insight into the possible role played by Ca^{2+} in the development of drug resistance in breast cancer, we performed a comparative high-content analysis of the intracellular Ca^{2+} dynamics in drug-sensitive human breast cancer MCF-7 cells and five drug-resistant, MCF-7-derived clonal cell lines. Fura-2 single cell ratiometric fluorescence microscopy was used to monitor real-time quantitative changes in cytosolic-free Ca^{2+} concentration ($[Ca^{2+}]_i$) upon addition of phosphoinositol-coupled receptor agonists. While the magnitude and the onset kinetics of the $[Ca^{2+}]_i$ rise were similar in drug-sensitive and drug-resistant cell lines, the decay kinetics of the $[Ca^{2+}]_i$ increase was found to be consistently slower in drug-resistant than drug-sensitive cells. Such a delay in reestablishing homeostatic $[Ca^{2+}]_i$ persisted in the absence of extracellular Ca^{2+} and was independent of the expression or function of specific drug efflux pumps associated with drug resistance. Moreover, intracellular Ca^{2+} pools releasable by phosphoinositol-coupled receptor agonists or thapsigargin appeared to be differentially shared in drug-sensitive and drug-resistant cells. In light of the clinical relevance that drug resistance has in the treatment of cancer, the molecular and biochemical relationship between alterations in Ca^{2+} dynamics and drug resistance demands to be further investigated and tested in a wider array of cell types. Automated microscopy will help greatly in this pursuit by facilitating both sample imaging and data analysis, thus allowing high-content as well as high-throughput screening of large sample sets. A protocol for studying $[Ca^{2+}]_i$ kinetics with a commercially available automated imaging platform is described.

Introduction

Human breast cancer cell lines (bcc) selected for resistance to antineoplastic agents are a valuable research tool for studying the mechanisms associated with the development of drug resistance, the major cause for

METHODS IN ENZYMOLOGY, VOL. 414

0076-6879/06 $35.00
DOI: 10.1016/S0076-6879(06)14018-5

chemotherapy failure in breast cancer patients. *In vitro*, drug-resistant (DR) bcc exhibit numerous differential biochemical features when compared to drug-sensitive (DS) cells. These include overexpression of various membrane drug efflux pumps (e.g., P-glycoprotein [P-gp], multidrug resistance-associated protein [MRP], and breast cancer resistance protein [BCRP], Barrand *et al.*, 1997; Doyle *et al.*, 1998), reduced susceptibility to apoptosis (Ogretmen and Safa, 1996), altered enzyme activity (Herman *et al.*, 2006), and gene expression (Kudoh *et al.*, 2000; Rahbar and Fenselau, 2005). Ca^{2+} is a ubiquitous intracellular molecule involved in the control of vital cellular processes and, thus, its spatial and temporal dynamics are finely controlled (Berridge *et al.*, 2003). Little is known, however, about the potential role played by Ca^{2+} in breast cancer drug resistance. Higher resting intracellular Ca^{2+} levels ($[Ca^{2+}]_i$) and deficient intracellular Ca^{2+} pools have been described in two separate lines of human breast cancer MCF-7 cells resistant to doxorubicin (Chen *et al.*, 2002; Mestdagh *et al.*, 1994). Interestingly, the epidermal growth factor receptor, whose activation leads to increased $[Ca^{2+}]_i$, is overexpressed in adriamycin-resistant MCF-7 cells but returns to the expression level exhibited by DS parental cells when chemosensitivity is restored (Dickstein *et al.*, 1993). Finally, drug resistance can be reversed by compounds that, albeit through different mechanisms, modulate Ca^{2+} dynamics independently. Verapamil (VER, a well-known voltage-operated Ca^{2+} channel and Ca^{2+} influx blocker) and cyclosporin A (an inhibitor of calcineurin, a Ca^{2+} calmodulin-dependent protein phosphatase shown to potentiate Ca^{2+} responses; Bandyopadhyay *et al.*, 2000; LoRusso *et al.*, 1997) are widely studied chemosensitizers in tumors overexpressing P-gp (Barrand *et al.*, 1997; Hall *et al.*, 1999; Twentyman *et al.*, 1990). Probenecid (an organic anion transport blocker shown to either depress or increase Ca^{2+} responses; DiVirgilio *et al.*, 1990; Packham *et al.*, 1996) and genistein (a protein tyrosine kinase inhibitor reported to prevent capacitative Ca^{2+} entry; Foster and Conigrave, 1999) are examples of compounds that modulate MRP pumps (Gollapudi *et al.*, 1997; Versantvoort *et al.*, 1993).

This chapter describes a protocol to identify potential differences in Ca^{2+} dynamics between DS and DR bcc. We chose single-cell fluorescence microscopy-based high-content analysis (HCA) as a tool for our investigation. This technology offers significant advantages over both fluorimetric Ca^{2+} measurements and whole-well, end-point plate reader-based high-throughput Ca^{2+} assays (e.g., FLIPR), as heterogeneous single-cell responses can be appreciated, real-time Ca^{2+} kinetics (rather than just the peak response) and spatially localized Ca^{2+} signals can be evaluated, and simultaneous analysis of other biological responses can be performed (DeBernardi and Brooker, 1996). Automated microscopy instrumentation

allows the processing of high volumes of samples, thus moving HCA into a higher throughput mode (high-content screening, HCS). Here, we describe in detail a procedure for HCA of Ca^{2+} kinetics in DS and DR bcc and provide a protocol to apply this HCA to a commercially available, automated imaging station for HCS purposes.

High-Content Analysis of Ca^{2+} Dynamics by Fluorescence Microscopy

Human Breast Cancer Cell Lines

Three different wild-type MCF-7 cell lines (wt, DS bcc) are tested and are from American Type Culture Collection (ATCC, Manassas, VA), the Lombardi Cancer Center, Georgetown University (GU), Washington, DC, and Dr. Susan Bates, NCI, NIH (Bethesda, MD). Five drug-resistant MCF-7-derived cell lines are used: MCF-7/ADR cells [resistant to adriamycin (Vickers *et al.,* 1988) and overexpressing P-gp (Fairchild *et al.*, 1987)]; MCF-7/VP cells (resistant to VP-16 etoposide and overexpressing MRP; Schneider *et al.,* 1994); MCF-7/C4 (resistant to camptothecin and not overexpressing P-gp or MRP; Fujimori *et al.,* 1996); MCF-7/Melph cells (resistant to melphalan and expressing neither P-gp nor MRP; Moscow *et al.*, 1993); and MCF-7/Ad-Vp cells [resistant to adriamycin and VER and expressing BCRP (Doyle *et al.*, 1998) but not P-gp or MRP (Lee *et al.*, 1997)]. Cells are grown at 37° in a humidified atmosphere of 95% air/5% CO_2, refed twice a week, and passaged once a week (not to exceed 80% confluence). DR cells are grown in the presence of the appropriate drug (in μM) : MCF-7/ADR–doxorubicin, 2; MCF-7/VP–VP-16 etoposide, 4; MCF-7/Melph–melphalan, 6; MCF-7/Ad-Vp 3000–doxorubicin, 5; and VER, 10. Pairs of DS and DR clones are plated and imaged the same day; we compared MCF-7/ADR and MCF-7/Ad-Vp cells with their parental DS lines from GU and NIH, respectively, and the other DR clones with MCF-7 cells from ATCC.

Media and Reagents

1. IMEM medium, 10% fetal calf serum, 2 m*M* L-glutamine, 100 U/ml penicillin, 100 μg/ml streptomycin, and 50 μg/ml gentamycin. Used for all cell lines except MCF-7/C4.
2. RPMI-1640 with 5% fetal calf serum, 1 m*M* nonessential amino acids, 0.1 m*M* sodium pyruvate, 2 m*M* L-glutamine, 100 U/ml penicillin, 100 μg/ml streptomycin, and 50 μg/ml gentamycin. Used only for MCF-7/C4 cells.
3. H/H buffer (Ham's F-10 medium supplemented with 20 m*M* Na-HEPES, pH 7.4)

4. Fura 2-AM (1 m*M* stock in anhydrous DMSO; store at –20°)
5. Fura-2 standards: 5 μM Fura-2 pentaK (10 m*M* stock in H_2O) in 10 m*M* Na-HEPES, pH 7.4, with either 1 m*M* $CaCl_2$ ("high" standard) or 1 m*M* EGTA tetrasodium salt ("low" standard).

Ca^{2+} Imaging

$[Ca^{2+}]_i$ is measured by Fura-2 fluorescence ratio imaging. Fura-2 is a dual-excitation, single-emission Ca^{2+} indicator that, by virtue of its ratiometric properties, allows quantitative Ca^{2+} measurements that are independent of artifacts such as uneven cell loading and intracellular dye distribution, wavelength and intensity of the excitation light, dye leakage, and photobleaching.

Cell Growth and Labeling

1. Plate cells (20,000 cell/ml) on 25-mm-round, thickness No.1 glass coverslips (Fisher Scientific) in six-well plates and grow for 48 to 72 h (60 to 70% confluence). To avoid artifacts in $[Ca^{2+}]_i$ measurements, grow DR cells in drug-free medium during this time.
2. Label cells with 5 μM Fura-2 AM (1 ml/well) in growth medium (45 min/37°).
3. Wash cells twice with H/H buffer (1 ml/well) and let sit for 15 min at room temperature to allow complete dye deesterification.
4. Transfer coverslips to stainless-steel chambers (Attofluor Coverlips Holder, Molecular Probes), fitting the microscope stage holder (H/H buffer volume = 950 μl/chamber).
5. Manually add compounds (20× in H/H buffer) to the chambers in 50-μl volumes to ensure fast diffusion over the cells being imaged.

Fluorescence Microscopy

Cells are imaged at room temperature using an Attofluor RatioVision fluorescence microscopy system (Atto Instruments, Rockville, MD) equipped with a Zeiss Axiovert 135 microscope, a F-Fluar 40×, 1.3 NA, oil-immersion objective, and an ICCD camera (high gain used for MCF-7/ADR and Ad/Vp cells). Fura-2 dual excitation ratio imaging is performed with emission at >510 nm and excitation at 340 nm (maximal signal with high $[Ca^{2+}]_i$) and 380 nm (maximal signal with low $[Ca^{2+}]_i$); the 340/380-nm excitation ratio increases as a function of the $[Ca^{2+}]_i$. Accurate day-to-day comparison of $[Ca^{2+}]_i$ is ensured by calibrating the instrument daily. A two-point calibration is done *in vitro* using 5 μM Fura-2 pentaK

standards (''high'' standard: maximal emission at 340 nm; ''low'' standard: maximal emission at 380 nm). Ratio values are converted by the software to $[Ca^{2+}]_i$ n*M* according to the equation described by Grynkiewicz *et al.* (1985), with a K_d of 225 n*M*.

Data Capture and Statistical Analysis

To identify single cells, regions of interests (ROIs) are placed manually and $[Ca^{2+}]_i$ is recorded over time (2-s interval) from each ROI. Thirty to 99 cells per microscopic field/coverslip are imaged simultaneously. Single-cell responses can be averaged to yield $[Ca^{2+}]_i$ population means ($\pm$ SEM) and plotted against time. Statistical analyses use the two-tailed, unpaired *t* test with a 95% confidence interval for differences between means (StatMate, GraphPad Software, San Diego, CA).

Ca^{2+} Elevating Agents

The status of the intracellular Ca^{2+} pool and Ca^{2+} mobilization from the endoplasmic reticulum (ER) are studied by either activating ER inositol 1,4,5- trisphosphate (IP_3) receptors [ATP and UTP (50 μM), bradykinin (BK, 10 μM), α-thrombin (THR, 5 μM) are phosphoinositol (PI)-coupled receptor agonists, which activate IP_3 receptors and Ca^{2+} release] or bypassing the PI pathway using thapsigargin (TG, 1 μM), which poisons ER Ca^{2+}-ATPase pumps, thus preventing the reuptake into the stores of Ca^{2+} passively diffused out into the cytosol (Tharstrup *et al.*, 1990).

Measurement of Resting Ca^{2+} State and Stimulated $[Ca^{2+}]_i$ Response

Resting $[Ca^{2+}]_i$ is recorded for ~60 s before agonist addition and ranges between 40 and 70 n*M* with no statistically significant differences detected among the three DS MCF-7 cell lines and between DS and DR cells, although DR cells exhibit a wider range of variability (data not shown). MCF-7/ADR and MCF-7/Ad-Vp cells show a lower fluorescence signal than the other cell lines, likely reflecting a high degree of dye extrusion by the drug efflux pumps (Homolya *et al.*, 1993); however, pump inhibitors are not used during dye loading to avoid affecting the native Ca^{2+} responses of the cells. The number of cells responsive to a given agonist varies among all the cell lines with <30% of the cells (both DS and DR) responding to THR and BK, whereas >95% of the cells (both DS and DR) consistently respond to ATP and UTP (Dixon *et al.*, 1997). Onset kinetics are comparable among all the DS and DR cell lines and rather fast [average onset $t_{1/2}$ (time to reach 50% of the $[Ca^{2+}]_i$ peak) is ~10 s, Fig. 1]. The magnitude of the

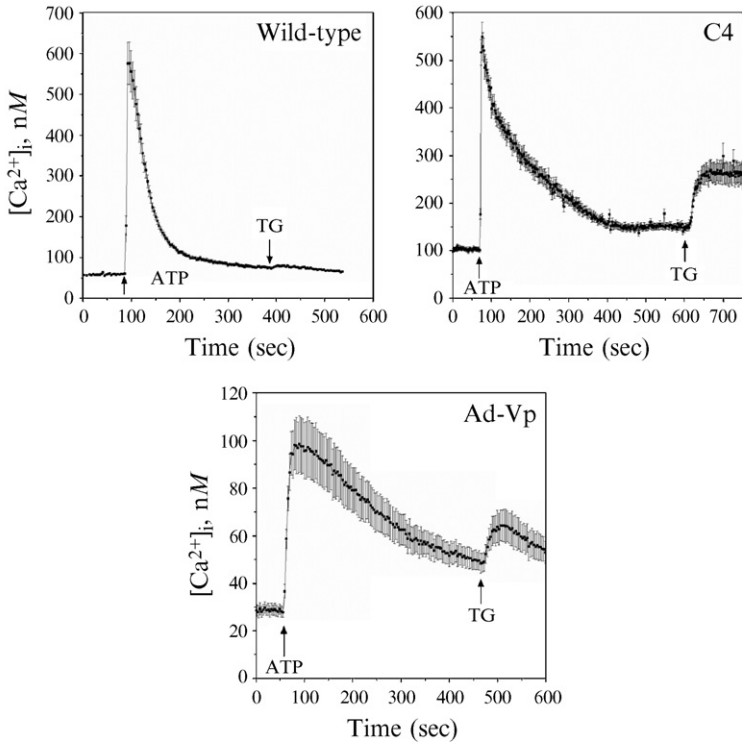

FIG. 1. HCA of intracellular Ca^{2+} kinetics in wild-type MCF-7 cells and two representative MCF-7-derived drug-resistant cell lines. ATP (50 μM) and then TG (1 μM) were added as indicated by arrows. Ca^{2+} responses from 30 to 99 individual cells were monitored simultaneously; data are presented as population means ± SEM. of $[Ca^{2+}]_i$ in nM values. In the experiments shown, ATP-induced $[Ca^{2+}]_i$ decay $t_{1/2}$ (calculated as described in the text) were: wild-type cells, 34 s; C4 cells, 84 s; Ad-Vp cells, 164 s. Ca^{2+} traces from each cell line are representative of at least 10 experiments.

response (fold increase = peak $[Ca^{2+}]_i$ /basal $[Ca^{2+}]_i$ varies among DS and DR cells depending on the agonist (Table I). All three MCF-7 wt cell lines respond to any given agonist with similar magnitude and, thus, data shown represent pooled responses. With selected agonists, quantitative differences in peak $[Ca^{2+}]_i$ are observed between DS and DR cells, which, however, are found not to be statistically significant (Table I). MCF-7/ADR cells pre-treated with VER (25 μM, 2 h) show a significantly enhanced dye loading and magnitude of the ATP-evoked Ca^{2+} (fold increase: MCF-7/ADR no VER: 1.5 ± 0.2, $n = 5$; with VER: 3.9 ± 0.7, $n = 9$, $P < 0.05$).

TABLE I
FOLD $[Ca^{2+}]_i$ INCREASE EVOKED BY VARIOUS AGONISTS IN HUMAN BREAST CANCER CELL LINES

	ATP	UTP	BK	THR	TG
Drug-sensitive cells					
MCF-7 wt	7.9 ± 1.8[a] ($n = 67$)	6.0 ± 1.3 ($n = 9$)	4.1 ± 0.8 ($n = 16$)	2.8 ± 0.1 (n = 3)	2.8 ± 0.5 ($n = 21$)
MDA-MB-231	16.5 ± 4.8 ($n = 10$)	n.d.[b]	6.5 ± 1.8 ($n = 3$)	13.5 ± 5.1 ($n = 3$)	3.5 ± 0.9 ($n = 3$)
Drug-resistant cells					
MCF-7/ADR	2.9 ± 0.7 ($n = 25$)[c]	2.2 ± 0.3 ($n = 3$)[d]	1.9 ± 0.5 ($n = 3$)[e]	2.8 ± 1.1 ($n = 3$)	2.7 ± 0.7 ($n = 10$)
MCF-7/AdVp	4.5 ± 1.2 ($n = 12$)	3.7 ± 0.8 ($n = 3$)	3.5 ± 1.0 ($n = 7$)	n.d	2.4 ± 0.7 ($n = 11$)
MCF-7/VP	4.4 ± 1.2 ($n = 11$)	5.2 ± 1.9 ($n = 3$)	3.3 ± 1.7 ($n = 3$)	n.d.	1.5 ± 0.1 ($n = 6$)[f]
MCF-7/C4	5.9 ± 0.8 ($n = 12$)	n.d.	3.0 ± 0.6 ($n = 3$)	3.3 ± 0.3 ($n = 3$)	3.4 ± 0.8 ($n = 7$)
MCF-7/Melph	16.0 ± 6.1 ($n = 17$)[g]	3.7 ± 0.3 ($n = 5$)	n.d.	n.d.	n.d.

[a] Mean ± SEM.
[b] Not determined.
[c] $P = 0.0976$ versus ATP response in DS MCF-7 cells.
[d] $P = 0.1341$ versus UTP response in DS MCF-7 cells.
[e] $P = 0.2030$ versus BK response in DS MCF-7 cells.
[f] $P = 0.1834$ versus TG response in DS MCF-7 cells.
[g] $P = 0.0841$ versus ATP response in DS MCF-7 cells.

All cell lines responded to TG when applied as the first drug, with a comparable ~3-fold $[Ca^{2+}]_i$ increase (Table I). As expected from the mode of action of TG, onset Ca^{2+} kinetics ($t_{1/2}$ ~40 s) are slower than those evoked by PI-coupled receptor agonists but are similar in DS and DR bcc. Interestingly, in four DR clones, but not in MCF-7 wt or MCF-7/Vp cells (the only DR clone with receptor-mediated $[Ca^{2+}]_i$ decay similar to wt cells), TG increased $[Ca^{2+}]_i$ when applied after ATP (Fig 1). Also, selected DR clones are able to respond to ATP after TG induced a robust $[Ca^{2+}]_i$ increase (authors' personal communication). Thus, the DS and DR bcc under study exhibit similar Ca^{2+} homeostatic levels and comparably filled IP_3- and TG-sensitive intracellular stores that release Ca^{2+} (via active IP_3 release or constitutive leakage) with seemingly equal efficiency and kinetics. However, TG- and IP_3-releasable pools seem to be shared differentially in DS and DR bcc and differential sensitivity to TG of the ER Ca^{2+}-ATPase pumps may exist.

Decay Kinetics of Agonist-Stimulated $[Ca^{2+}]_i$ Response

The decay kinetics of $[Ca^{2+}]_i$ increased by all PI-coupled receptor agonists are markedly slower in four out of five DR MCF-7 clones than in DS bcc (Figs. 1 and 2). Also, single-cell HCA of Ca^{2+} kinetics revealed greater variation in cell behavior among DR than DS cells, as reflected by larger data error bars (Fig. 1). To quantify Ca^{2+} decay, we used the $[Ca^{2+}]_i$ decay $t_{1/2}$, calculated as the time (seconds) at which $[Ca^{2+}]_i$ reaches 50% of the peak during the decay phase, *minus* the time at which the $[Ca^{2+}]_i$ peak is achieved. Compared to DS cells, (1) MCF-7/ADR and MCF-7/Ad-Vp cells showed the longest decay $t_{1/2}$, (2) MCF-7/C4 and MCF-7/Melph cells exhibited a decay $t_{1/2}$ about twice as long, and (3) MCF-7/VP cells showed a decay $t_{1/2}$, which, for all the agonists tested, was consistently, although not significantly, longer (Figs. 1 and 2). Importantly, even a 24-h treatment with VER (25 μM) did not accelerate ATP-evoked Ca^{2+} decay $t_{1/2}$ in MCF-7/ADR (MCF-7 wt: 46 ± 6.3 s, $n = 9$; MCF-7/ADR: 132 ± 20 s, $n = 9$; $P = 0.0008$). Chelation of extracellular Ca^{2+} by EGTA did not significantly affect the magnitude of ATP responses (indicating that the primary cause for the $[Ca^{2+}]_i$ increase is ion mobilization from internal stores) but accelerated the $[Ca^{2+}]_i$ decay in both DS and DR cells; nevertheless, decay kinetics in DR cells remained significantly longer than DS cells (data not shown). In both DS and DR bcc, $[Ca^{2+}]_i$ increased by TG was slower to return to baseline than the receptor-mediated $[Ca^{2+}]_i$ rise. In particular, two DR clones (Ad-Vp and VP cells) showed a significantly slower recovery than DS cells (authors' personal communication).

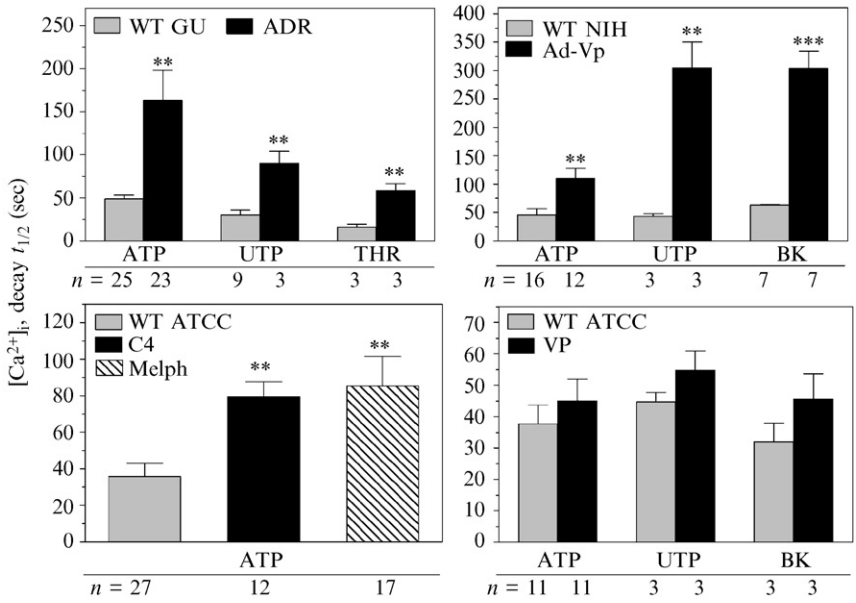

FIG. 2. Summary of $[Ca^{2+}]_i$ decay $t_{1/2}$ in wild-type and drug-resistant MCF-7 cells following exposure to PI-coupled receptor agonists. The source of the various DS MCF-7 lines is indicated. The decay $t_{1/2}$ of the $[Ca^{2+}]_i$ increase evoked by each agonist was calculated as described in the text. Data are means ± SEM. n = number of experiments. $^{**}P<0.01$, $^{***}P< 0.001$ indicate decay $t_{1/2}$ significantly different from wild-type cells. Thirty to 99 individual cells were imaged per experiment.

Conclusions from HCA and Rationale for High-Content Screening

Single-cell, real-time HCA of intracellular Ca^{2+} dynamics identified slower $[Ca^{2+}]_i$ decay kinetics in DR bcc when compared to DS bcc. This phenomenon does not correlate with the functional expression of known drug efflux pumps, occurs after IP_3-dependent and -independent Ca^{2+} increase, and thus localizes downstream from specific Ca^{2+}-signaling pathways, suggesting that DR bcc are impaired in their ability to readily remove Ca^{2+} accumulated in the cytosol and restore Ca^{2+} homeostasis.

Ca^{2+} transients (''on'' reaction) are biphasic, consisting of a rapid-onset phase (release from intracellular stores) and a slower compensatory influx (capacitative entry; Berridge *et al.*, 2003) that amplifies the initial Ca^{2+} signal and replenishes the stores. A recovery phase (''off ''reaction) then follows when cells rectify the increased $[Ca^{2+}]_i$ via Ca^{2+} binding to cytoplasmic proteins (both buffer and effector proteins), Ca^{2+} efflux (through

plasmalemmal Ca^{2+}-ATPase pumps and $Na^{+}Ca^{2+}$ exchangers), and Ca^{2+} sequestration into the stores (through ER Ca^{2+}-ATPase pumps and mitochondrial Ca^{2+} transporters). Thus, any of these ''off'' mechanisms could be impaired in the DR bcc tested in this study.

While sporadic reports imply a potential association between some of these mechanisms and drug resistance in cancer (e.g., McAlroy *et al.,* 1999; Padar *et al*., 2004; Villa and Doglia, 2004; Zhou *et al.*, 2006), no systematic studies are available where DS and DR bcc are interrogated for possibly causal links between any of these mechanisms and drug resistance. In view of the clinical relevance that drug resistance has in breast cancer therapy, further investigations are needed to (1) identify the mechanism(s) responsible for the slower decay, (2) study the specificity and occurrence of anomalous Ca^{2+} dynamics in a wider array of DR cancer cells, and (3) establish a potential relationship (cause/effect) between Ca^{2+} and drug resistance. Such studies call for higher cell imaging and data analysis throughput than HCA can provide. HCS of Ca^{2+} dynamics and automated microscopy will make these studies feasible.

High-Content Screening

In our laboratory, automated fluorescence microscopy is performed on a BD Pathway Bioimager (BD Bioscience, Rockville, MD), which displays advantageous features that facilitate the HCS studies we propose as well as other HCA kinetic and end point applications (Chan *et al.,* 2005; DeBernardi *et al*., 2006). Relevant to our project, this system uses mercury arc lamps as light sources, which, combined with 340- to 380-nm excitation filters and a UV transmission-optimized 20× objective, 0.75 NA, provide optimal excitation for Fura-2 and, compared to laser-based systems, minimizes photobleaching and phototoxicity greatly (a major concern when imaging live cells). A high-sensitivity CCD camera, with adjustable gain, affords detection of suboptimal emission signals (such as those exhibited by DR bcc overexpressing drug efflux pumps). The imaging station has environmental control (5% CO_2 and 37° ensure physiological conditions for live cells) and an on-stage fluidic head (with disposable tips) for automated compound addition compatible with 96-well plates (high-density plates provide high sample throughput). Because the stage is stationary and the objective moves underneath the 96-well plate, imaging takes place while compounds are added and, thus, changes in early-onset Ca^{2+} kinetics can be detected. The software (AttoVision) performs an automated autofocus routine, segmentation [single cells are identified as ROIs (virtually unlimited number)], image capture, drug addition, ratio calculations, and real-time data display. To increase sample throughput, multiple wells within a

96-well plate can be interleaved and processed at the same time [the x–y mechanical resolution (100 nm) allows the objective to reposition accurately on previously imaged fields] with user-settable time spacing between imaging and fluidic steps. Further improvement in throughput can be achieved by performing cell segmentation and data analysis off-line (Reanalysis Option), after the entire plate is processed. To perform HCS on bcc, we are in the process of adapting our HCA Ca^{2+} kinetics on the Pathway. Here we describe the modifications to the HCA protocol, the advantages offered by the automated data analysis, and provide sample data obtained with rat C6 glioma cells, which we use routinely for Ca^{2+} kinetics studies.

Cell Plating, Labeling, and Imaging Setup

1. Plate cells in 96-well plastic plates (Greiner Bio-one, μClear black wall plates) at a density of 5000 to 10,000 cell/well (100 μl/well) and grow cells 24 to 48 h prior to imaging.

2. Label cells as described for HCA (loading: 60 μl/well dye solution; washing: 100 μl/well H/H buffer; imaging: 80 μl/well H/H buffer).

3. Prepare compounds (5$\times$ in H/H buffer) and place in specific wells of a 96-well conical-bottom, polypropylene plate; automated delivery of 20 μl/well volumes at a rate of 40 μl/s ensures even diffusion over the cells with no need for mechanical mixing.

4. To calibrate the instrument, place the two Ca^{2+} standards (100 μl/well) in adjacent wells of a Greiner plate. Open the Dye Setup dialog box (Calibration Tab) and capture >510-nm emissions after excitation at 340 (numerator) or 380 (denominator) nm of the high or low standards, respectively, and set exposure times to yield maximal signal with either standard (usually, denominator exposure time is twice that of the numerator); the software uses the captured ratio and intensity values to generate a calibration curve and interpolate ratio values into $[Ca^{2+}]_i$ (Grynkiewicz *et al.*, 1985).

5. Set up and save a Fura-2 Ca^{2+} ratio-imaging ''template macro'' and apply it to all the wells to be processed—''compound macro''; this macro is indeed an automated assay protocol listing all the various steps to be performed in each well.

- Autofocus setup course and fine; define the best algorithm (e.g., Vollath F4), the maximal z span that the objective must travel above/below starting z position, and the optimal z interval to ensure that focus on the cells is attained. Test at least a couple of wells on each side of the 96-well plate to determine best settings. These parameters are plate and cell type specific.

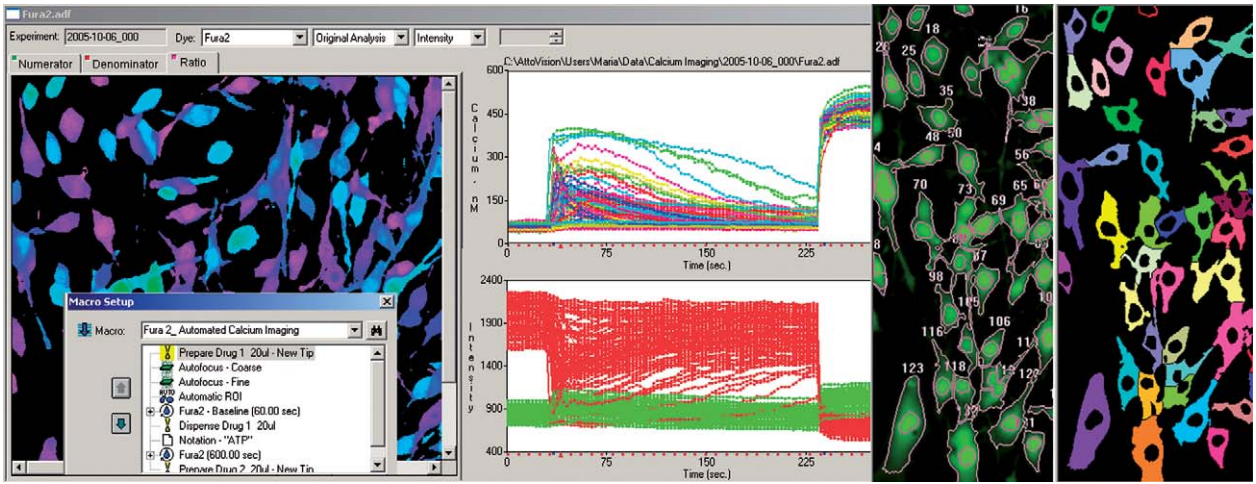

FIG. 3. HCS of Ca^{2+} kinetics with automated fluorescence microscopy. Screen shot from the Pathway Bioimager showing Ca^{2+} changes over time (seconds) in Fura-2-labeled C6 cells exposed to ATPs (50 μM) first and then to the Ca^{2+} ionophore, ionomycin (1 μM). The upper graph shows color-coded, single-cell Ca^{2+} responses (one trace = one cell; 106 cells being imaged) and the lower graph shows emission signals after 340-nm (green traces) and 380-nm (red traces) excitation. On the left side of the graphs, a pseudo-colored 340/380-nm ratio image of the cells highlights heterogeneity in the ATP responses (ratiometric color model scale for $[Ca^{2+}]_i$ level: purple/blue = low; green/yellow = high). Overlaid on this image is a screen shot capture of the Macro Setup dialog box showing the automated steps carried out in each well of the plate. The two panels on the right side of the graphs depict the automated segmentation process: using the dual channel exclude center option, single cells are identified as ROIs, numbered, and a segmentation mask is generated where the colors assigned to individual ROIs match those of the corresponding Ca^{2+} traces in the graph.

• Auto-ROI setup: use the dual channel/exclude center shape (which places ROIs on the cytoplasm excluding the nucleus) to segment single cells; reject dead or unhealthy cells by size (limiting object pixel min/max) and/or brightness (lowering upper threshold intensity). Use shading and watershed options to correct for uneven field illumination and improve segmentation if cells are too clustered.

• Imaging setting: in light path setup, define filter configuration: numerator A lamp = 340 and denominator B lamp = 380/ND, epifluorescence dichroic = 400DCLP, emission filter = 435 nm LP; in dye setup, define the exposure time (seconds) and camera gain for both 340- and 380-nm excitation (note that if working in calibrated mode, these parameters are set during the calibration procedure and cannot be changed for the calibration to remain valid) as well as the numerator and denominator threshold for ratio capture; in probe cycle, define sampling frequency (2 s) and duration of kinetic imaging (baseline and after compound addition).

• Fluid handling setup (prepare and dispense steps), define the volume (20 μl), rate of delivery (40 μl/s), origin, and destination well of each compound to be added to the cells.

6. Set up a treatment plate map indicating the agonist (and its concentration) added to each well to be processed and associate it with the macro. Assign the macro to the assay launch box. For daily use, launch the macro from here and adjust parameters such as exposure times, camera gain, and ROI settings to compensate (if necessary) for variation in cell labeling, morphology, and density. Create new treatment plate maps as needed.

Data Display, Analysis, and Report

1. Single cell kinetic responses from each ROI are analyzed on the fly (unless a reanalysis mode is chosen) and displayed in graphs showing changes over time in both the emission signals (after 340 and 380 nm excitation) and the 340/380-nm ratio (or $[Ca^{2+}]_i$, n*M* in calibrated mode).

2. Numbered ROIs in the images and their corresponding ratio traces in the graph are color coded and interactive; thus, ''clicking'' on a trace highlights the cell of origin and vice versa, allowing the identification of individual cell responses within a heterogeneous population (Fig. 3).

3. As the wells are processed, corresponding average traces are plotted on the plate map for immediate visualization. Each well is assigned an ADF file (proprietary binary format) containing measured numeric data (kinetic data points) and images saved during the experiment (TIFF files). Also, an experiment summary (text file) is generated that contains

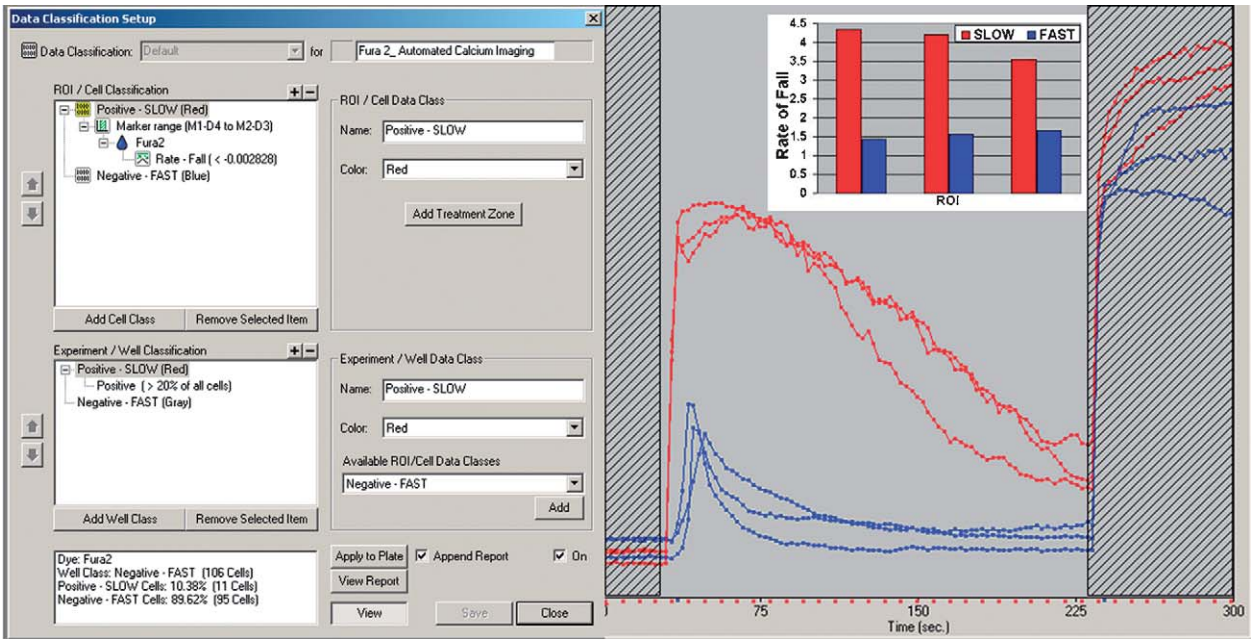

FIG. 4. HCS Ca^{2+} decay ROI data analysis. Screen shot from the Pathway Bioimager showing the ROI classification process, based on the ATP-increased Ca^{2+} rate-of-fall data attribute, applied to the experiment displayed in Fig. 3 (for clarity purpose, only six representative cell traces are shown). The data classification setup dialog box shows the treatment zone range (corresponding to the area between the two hatched regions on the graph) and the rate-of-fall setting. Ca^{2+} traces with decay slower than the preset value are classified as slow (red), whereas traces with faster decay are classified as fast (blue). An ROI Summary.txt file is generated with single cell rate-of-fall values. These values (negative integers) can then be transformed within Microsoft Excel or BD Image Data Explorer into positive integers and plotted.

	A	B	C	D	E	F	G
1	C:\AttoVision\Users\Maria\Data\Calcium Imaging\2005-11-21_007						
2							
3	DATA CLASSIFICATION DEFINITION						
4	**CELL CLASSES**						
5	**Cell Class 1 SlowDecay (Positive,Red)**						
6	__Marker range (M1+D1 to M2)						
7	____Fura2						
8	_____Rate - Fall (< -0.0045)						
9	**Cell Class 2 Fast Decay (Negative, Blue)**						
10	**WELL CLASSES**						
11	Well Class 1: Positive (Yellow)						
12	__Positive >30%						
13	Well Class 2: Negative (Gray)						
14							
15							
16	Well	**Well**	Total	Positive	Positive	Negative	Negative
17	ID	**Class**	Cells	Cells	Percentage	Cells	Percentage
18	----	-----	-----	--------	----------	--------	----------
19	**B02**	**Negative**	63	12	19.05%	51	80.95%
20	**B03**	**Positive**	75	41	54.67%	34	45.33%
21	**B04**	**Positive**	61	23	37.70%	38	62.30%
22							

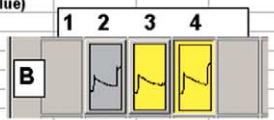

	A	B	C	D	E	F
1	BD Image Data Explorer					
2						
3	**WELL DATA REPORT:** Fura-2	Calcium Imaging				
4	**DATA SOURCES:**	2005-11-21_007				
5						
6		ATP	ROI Count	**Rate of Fall Transformed**		
7	Well ID			Average	Std Dev	Std Err
8	B002	50 µM	63	3.793326447	5.110702	0.64906
9	B003	50 µM	75	5.237246684	2.891212	0.336097
10	B004	50 µM	61	4.136270621	1.248917	0.161235
11						
12						
13						
14						
15						
16						
17						
18						
19						
20						
21						
22						

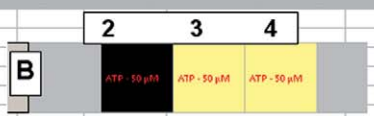

FIG. 5. HCS Ca^{2+} decay well data analysis and report. Data classification based on ATP-increased Ca^{2+} rate of fall is applied to a plate (three representative wells, B 2, 3, and 4 are shown). (Left) A Report.txt file is generated within AttoVision summarizing both ROI (percentage of positive and negative cells in each well) and well classification data (wells are considered positive and color coded in yellow if more than 30% of the ROIs exhibit a decay slower than the preset value; negative wells are displayed in gray). (Right) ROI summary and treatment plate map files are imported into the IDE program, which generates a plate report listing the average ± SD and SEM of the rate-of-fall values in each well analyzed and a plate heat map (B2, negative, fast decay = black; B3–4, positive, slower decay = yellow).

relevant assay parameter information about each experiment and can be used for documentation and data storage/mining.

4. Experimental data are binned into user-defined classes by using a hierarchical data classification structure wherein ROIs and wells are classified as positive or negative (and color coded accordingly) based on specific data attributes (amplitude [max/min/average], rate-of-rise [onset, slope of fluorescence intensity increase over time] or, as in our case, rate-of-fall [decay, slope of fluorescence intensity decrease over time]) over the entire data range or within specific treatment zones ($TZ_{1,2,3,n}$) (e.g., start to first compound addition [baseline], from compound addition to peak response, or, as in our case, from peak response back to baseline]). A preset data classification can be associated with the kinetic macro prior to running the experiment and all the ROIs and wells are then classified (and color coded accordingly) on the fly (Fig. 4).

5. For each experiment, an ROI summary (with single cell kinetic data and classification parameters) and a plate report (with percentage positive/negative wells) are automatically generated as text files and can be imported into traditional spreadsheet or graphing programs.

6. In our HCS, the ROI summary and treatment plate map files are imported into BD Image Data Explorer (IDE), a Microsoft Excel-based program that performs single cell-based data analysis and generates reports and charts (e.g., dose–response curves; EC_{50}, Z' and S/N calculations; histograms, scatter plots). Within IDE, new arithmetic parameters are created to, for example, normalize raw amplitude values (by diving peak ratio/basal ratio or peak $[Ca^{2+}]_i$ /basal $[Ca^{2+}]_i$) and transform rate-of-fall raw values (negative integers) into positive integers (more convenient to analyze and plot). Wells positive for the desired data attribute (in our case, a Ca^{2+} rate of fall less than a preset threshold value from drug-sensitive cells) are visually identifiable in a heat map, a pseudo-colored overview of the plate where both scale and color are user adjustable.

7. The final IDE report will show the rate-of-fall values (or the values of any chosen data attribute) per well (ROI average ±SD and SEM); user-generated graphs can be saved with this report, printed, and entered into hard-copy, record-keeping books (Fig. 5).

Acknowledgments

The authors are grateful to Drs. Bates, Moscow, Pommier, and Schneider for the precious gift of the drug-resistant MCF-7 clones. This work was supported in part by Grant ROI HL 28940 from NIH.

References

Bandyopadhyay, A., Shin, D. W., and Kim, D. H. (2000). Regulation of ATP-induced calcium release in COS-7 cells by calcineurin. *Biochem. J.* **348,** 173–181.

Barrand, M. A., Bagrij, T., and Neo, S. Y. (1997). Multidrug resistance-associated protein: A protein distinct from P-glycoprotein involved in cytotoxic drug expulsion. *Gen. Pharmacol.* **28,** 639–645.

Berridge, M. J., Bootman, M. D., and Roderick, H. L. (2003). Calcium signaling: Dynamics, homeostasis and remodelling. *Nature Rev. Mol. Cell Biol.* **47,** 517–529.

Chan, G. K., Richards, G. R., Peters, M., and Simpson, P. B. (2005). High content kinetic assay of neuronal signaling implemented on BD Pathway HT. *ASSAY Drug Dev. Technol.* **3,** 623–636.

Chen, J. S. K., Agarwal, N., and Mehta, K. (2002). Multidrug-resistant MCF-7 breast cancer cells contain deficient intracellular calcium pools. *Breast Cancer Res. Treat.* **71,** 237–247.

DeBernardi, M. A., and Brooker, G. (1996). Single cell Ca^{2+}/cAMP cross-talk monitored by simultaneous Ca^{2+}/cAMP fluorescence ratio imaging. *Proc. Natl. Acad. Sci. USA* **93,** 4577–4582.

DeBernardi, M. A., Hewitt, S. M., and Kriete, A. (2006). Automated confocal imaging and high-content screening for Cytomics. *In* ''Handbook of Biological Confocal Microscopy'' (J. B. Pawley, ed.), pp. 818–828. Springer Science, New York.

Dickstein, B., Valverius, E. M., Wosikowsky, K., Saceda, M., Pearson, J. W., Martin, M. B., and Bates, S. E. (1993). Increased epidermal growth factor receptor in an estrogen-responsive adriamycin-resistant MCF-7 cell line. *J. Cell Physiol.* **157,** 110–118.

DiVirgilio, F., Steinberg, T., and Silverstein, S. C. (1990). Inhibition of Fura-2 sequestration and secretion with organic anion transport blockers. *Cell Calcium* **11,** 57–62.

Dixon, C. J., Bowler, W. B., Fleetwood, P., Ginty, A. F., Gallagher, J. A., and Carron, J. A. (1997). Extracellular nucleotides stimulate proliferation in MCF-7 breast cancer cells via P2-purinoceptors. *Br. J. Cancer* **75,** 34–39.

Doyle, L. A., Yang, W., Abruzzo, L. V., Krogmann, T., Gao, Y., Rishi, A. K., and Ross, D. D. (1998). A multidrug resistance transporter from human MCF-7 breast cancer cells. *Proc. Natl. Acad. Sci. USA* **26,** 15665–15670.

Fairchild, C. R., Ivy, S. P., Kao-Shan, C. S., Whang-Peng, J., Rosen, N., Israel, M. A., Melera, P. W., Cowan, K. H., and Goldsmith, M. E. (1987). Isolation of amplified and overexpressed DNA sequences from adriamycin-resistant human breast cancer cells. *Cancer Res.* **47,** 5141–5148.

Foster, F. M., and Conigrave, A. D. (1999). Genistein inhibits lysosomal enzyme release by suppressing Ca^{2+} influx in HL-60 granylocytes. *Cell Calcium* **25,** 69–76.

Fujimori, A., Gupta, M., Hoki, Y., and Pommier, Y. (1996). Acquired camptothecin resistance in human breast cancer MCF-7/C4 cells with normal topoisomerase I and elevated DNA repair. *Mol. Pharmacol.* **50,** 1472–1478.

Gollapudi, S., Kim, C. H., Tran, B. N., Sangha, S., and Gupta, S. (1997). Probenecid reverses multidrug resistance in multidrug resistance-associated protein-overexpresssing HL60/AR and H69/AR cells but not in P-glycoprotein-overexpressing HL60/Tax and P388/ADR cells. *Cancer Chemother. Pharmacol.* **40,** 150–158.

Grynkiewicz, G., Poenie, M., and Tsien, R. Y. (1985). A new generation of Ca^{2+} indicators with greatly improved fluorescence properties. *J. Biol. Chem.* **260,** 3440–3450.

Hall, J. G., Cory, A. H., and Cory, J. H. (1999). Lack of competition of substrates for P-glycoprotein in MCF-7 cells overexpressing MDR1. *Adv. Enzyme Regul.* **39,** 113–128.

Herman, J. F., Mangala, L. S., and Mehta, K. (2006). Implications of increased tissue transglutaminase (TG2) expression in drug-resistant breast cancer (MCF-7) cells. *Oncogene* Jan 30 Epub ahead of print.

Homolya, L., Hollo, Z., Germann, U., Pastan, I., Gottesmann, M. M., and Sarkadi, B. (1993). Fluorescent cellular indicators are extruded by the multidrug resistance protein. *J. Biol. Chem.* **268,** 21493–21496.

Kudoh, K., Ramanna, M., Ravatn, R., Elkahloun, A. G., Bittner, M. L., Meltzer, P. S., Trent, J. M., Dalton, W. S., and Chin, K-V. (2000). Monitoring the expression profiles of doxorubicin-induced and doxorubicin-resistant cancer cells by cDNA microarray. *Cancer Res.* **60,** 4161–4166.

Lee, J. S., Scala, S., Matsumoto, Y., Dickstein, B., Robey, R., Zhan, Z., Altenberg, G., and Bates, S. E. (1997). Reduced drug accumulation and multidrug resistance in human breast cancer cells without associated P-glycoprotein or MRP overexpression. *J. Cell Biochem.* **65,** 513–526.

Lo Russo, A., Passaquin, A. C., Cox, C., and Ruegg, U. T. (1997). Cyclosporin A potentiates receptor-activated $[Ca^{2+}]_i$ increase. *J. Recept. Signal Transduct. Res.* **17,** 149–161.

McAlroy, H. L., Bovell, D. L., Plumb, J. A., Thompson, P., and Wilson, S. M. (1999). Drug extrusion,^{125} I-efflux and the control of intracellular Ca^{2+} in drug-resistant ovarian epithelial cells. *Exp. Physiol.* **84,** 285–297.

Mestdagh, N., Vandewalle, B., Hornez, L., and Henichart, J. P. (1994). Comparative study of intracellular calcium and adenosine 3′,5′-cyclic monophosphate levels in human breast carcinoma cells sensitive and resistant to adriamycin: Contribution to reversion of chemoresistance. *Biochem. Pharmacol.* **48,** 709–716.

Moscow, J. A., Swanson, C. A., and Cowan, K. H. (1993). Decreased melphalan accumulation in a human breast cancer cell line selected for resistance to melphalan. *Br. J. Cancer* **68,** 732–737.

Ogretmen, B., and Safa, A. R. (1996). Down-regulation of apoptosis-related bcl-2 but not bcl-xL or bax protein in multidrug-resistant MCF-7/Adr breast cancer cells. *Int. J. Cancer* **67,** 608–614.

Packham, M. A., Rand, M. L., Perry, D. W., Ruben, D. H., and Kinlough-Rathbone, R. L. (1996). Probenecid inhibits platelet responses to aggregating agents *in vitro* and has a synergistic inhibitory effect with penicillin G. *Thromb. Haemost.* **76,** 239–244.

Padar, S., van Breemen, C., Thomas, D. W., Uchizono, J. A., Livesey, J. C., and Rahimian, R. (2004). Differential regulation of calcium homeostasis in adenocarcinoma cell line A549 and its taxol-resistant subclone. *Br. J. Pharmacol.* **142,** 305–316.

Rahbar, A. M., and Fenselau, C. (2005). Unbiased examination of changes in plasma membrane proteins in drug resistant cancer cells. *J. Proteome Res.* **4,** 2148–2153.

Schneider, E., Horton, J. K., Yang, C. H., Nakagawa, M., and Cowan, K. H. (1994). Multidrug resistance-associated protein gene overexpression and reduced drug sensitivity to topoisomerase II in breast carcinoma MCF-7 cells selected for etoposide resistance. *Cancer Res.* **54,** 152–158.

Tharstrup, O., Cullen, P. J., Drobak, B. K., Hanley, M. R., and Dawson, A. P. (1990). Thapsigargin, a tumor promoter, discharges intracellular Ca^{2+} stores by specific inhibition of endoplasmic Ca^{2+}-ATPases. *Proc. Natl. Acad. Sci. USA* **87,** 2466–2470.

Twentyman, P. R., Reeve, J. G., Koch, G., and Wright, K. A. (1990). Chemosensitization by verapamil and cyclosporin A in mouse tumour cells expressing different levels of P-glycoprotein and CP22 (sorcin). *Br. J. Cancer* **62,** 89–95.

Versantvoort, C. H., Schuurhuis, G. J., Pinedo, H. M., Eekman, C. A., Kuiper, C. M., Lankelma, J., and Broxterman, H. J. (1993). Genistein modulates the decreased drug

accumulation in non-P-glycoprotein mediated multidrug resistant tumour cells. *Br. J. Cancer* **68,** 939–946.

Vickers, P. J., Dickson, R. B., Shoemaker, R., and Cowan, K. H. (1988). A multidrug-resistant MCF-7 breast cancer cell line which exhibits cross-resistance to antiestrogens and hormone-independent tumor growth *in vivo*. *Mol. Endocrinol.* **2,** 886–892.

Villa, A. M., and Doglia, S. M. (2004). Mitochondria in tumor cells studied by laser scanning confocal microscopy. *J. Biomed. Opt.* **9,** 385–394.

Zhou, Y., Xu, Y., Qi, J., Xiao, Y, Yang, C., Zhu, Z., and Xiong, D. (2006). Sorcin, an important gene associated with multidrug-resistance in human leukemia cells. *Leuk. Res.* **30,** 469–476.

[19] Measurement and Analysis of Calcium Signaling in Heterogeneous Cell Cultures

By GILLIAN R. RICHARDS, ANDREW D. JACK, AMY PLATTS, and PETER B. SIMPSON

Abstract

High-content imaging platforms capable of studying kinetic responses at a single-cell level have elevated kinetic recording techniques from labor-intensive low-throughput experiments to potential high-throughput screening assays. We have applied this technology to the investigation of heterogeneous cell cultures derived from primary neural tissue. The neuronal cultures mature into a coupled network and display spontaneous oscillations in intracellular calcium, which can be modified by the addition of pharmacological agents. We have developed algorithms to perform Fourier analysis and quantify both the degree of synchronization and the effects of modulators on the oscillations. Functional and phenotypic experiments can be combined using this approach. We have used post-hoc immunolabeling to identify subpopulations of cells in cocultures and to dissect the calcium responses of these cells from the population response. The combination of these techniques represents a powerful tool for drug discovery.

Introduction

High-content screening has become established as a valuable tool for drug discovery, allowing rapid quantification of end point parameters such as neurite outgrowth (Simpson *et al.*, 2001), cell motility (Richards *et al.*, 2004), and intracellular translocations (Ding *et al.,* 1998) that were previously not amenable to high-throughput screening. While these fixed end

METHODS IN ENZYMOLOGY, VOL. 414

0076-6879/06 $35.00
DOI: 10.1016/S0076-6879(06)14019-7